11th International Symposium on Turbulence and Shear Flow Phenomena (TSFP11)
Southampton, UK, July 30 to August 2, 2019

INVESTIGATING RAYLEIGH–BÉNARD CONVECTION AT LOW PRANDTL NUMBERS USING ONE-DIMENSIONAL TURBULENCE MODELING

Marten Klein
Department of Numerical Fluid and Gas Dynamics
BTU Cottbus-Senftenberg
Siemens-Halske-Ring 14, D-03046 Cottbus, Germany
marten.klein@b-tu.de

Heiko Schmidt
Department of Numerical Fluid and Gas Dynamics
BTU Cottbus-Senftenberg
Siemens-Halske-Ring 14, D-03046 Cottbus, Germany
heiko.schmidt@b-tu.de

ABSTRACT

The Rayleigh-number (Ra) dependence of the heat transfer in turbulent Rayleigh–Bénard convection at low Prandtl numbers (Pr) is numerically investigated with the stochastic one-dimensional turbulence (ODT) model. Its dimensionally reduced setting allows to reach $Ra = 10^{13}$ for $Pr = 0.021$ and $Ra = 10^{16}$ for $Pr = 0.7$ for samples with notionally infinite aspect ratio on state-of-the-art workstations. We estimate the model parameters for each Pr but keep them fixed when Ra is varied in order to assess the predictive capabilities of this model for highly turbulent flows. Present ODT results exhibit various effective Nusselt number (Nu) scalings $Nu \propto Ra^{\gamma}$. The exponent changes from $\gamma \approx 1/3$ to $\approx 1/2$ when Ra increases beyond the critical value $Ra_* \simeq 6 \times 10^{11}$ ($Pr = 0.021$) and $Ra_* \simeq 6 \times 10^{14}$ ($Pr = 0.7$), respectively. This is consistent with the transition to the ultimate regime. With the aid of ODT we show the presence of a turbulent boundary layer. The onset of the ultimate regime appears to be correlated with the formation of a well-developed logarithmic layer and relative enhancement of the turbulent temperature flux towards the bulk.

INTRODUCTION

Rayleigh–Bénard (RB) convection is a canonical problem for buoyancy-driven flows that are encountered in various applications ranging from technological to geophysical scales (e.g. Chillà & Schumacher, 2012). Figure 1 shows cylindrical and rectangular RB configurations. The vertical and lateral length scales are L and $D = 2R$ so that $\Gamma = D/L$ is the aspect ratio. Fluid is confined between the heated wall (T_{hw}) at the bottom and the cooled wall (T_{cw}) at the top.

For $\Gamma \to \infty$ the flow is governed by two dimensionless control parameters, the Rayleigh number Ra and the Prandtl number Pr:

$$Ra = \frac{g\beta\,\Delta T\,L^3}{\nu\kappa} \qquad Pr = \frac{\nu}{\kappa} \tag{1}$$

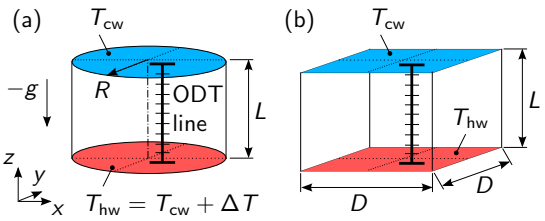

Figure 1. Schematics of (a) cylindrical and (b) rectangular Rayleigh–Bénard (RB) configurations. One-dimensional turbulence (ODT) simulations are carried out for a representative wall-normal vertical line ('ODT line').

In these expressions g is the background gravity, whereas ν, κ and β denote the kinematic viscosity, thermal diffusion and thermal expansion coefficients, respectively. Ra and Pr encompass several orders of magnitude in applications. Ra reaches easily up to 10^{27} and Pr takes values in between 10^{-7}–10^{23} (Chillà & Schumacher, 2012). We consider various Ra for $Pr = 0.7$ (air) and $Pr = 0.021$ (mercury).

The heat transfer is an important global property that depends crucially on the flow state. In non-dimensional form it is expressed as the Nusselt number Nu, which is given by (e.g. Scheel & Schumacher, 2014):

$$Nu = \frac{Q}{Q_{\mathrm{c}}} = 1 + \frac{\langle w'T'\rangle_{V,t}}{\kappa\Delta T/L} \tag{2}$$

In this equation, Q denotes the total and Q_{c} the purely conductive heat transfer. The rightmost expression relates Nu to the turbulent temperature flux per unit area, $\langle w'T'\rangle_{V,t}$, where V denotes volume and t temporal averaging under statistically stationary conditions.

For increasing Ra, the buoyancy forcing increases so that the boundary layer will eventually become fully turbulent. This is the transition from the classical to the ultimate

state of convection (Kraichnan, 1962; Grossmann & Lohse, 2000). The transition manifests itself by an increase of the scaling exponent in $Nu \propto Ra^{\gamma}$ from $\gamma \approx 1/3$ (Malkus, 1954) to $1/2$ (Kraichnan, 1962).

For $Pr \simeq 1$, there is evidence from laboratory experiments that the transition occurs around the critical value $Ra_* \simeq 10^{14}$ (Chillà & Schumacher, 2012; He *et al.*, 2012). It has been argued, however, that the $Nu \propto Ra^{1/2}$ scaling might also be due to roughness (Zhu *et al.*, 2019) or non-Oberbeck–Boussinesq effects in laboratory experiments (Urban *et al.*, 2019). Three-dimensional direct numerical simulations (3-D DNSs) for smooth walls and Boussinesq fluids have remained in the classical regime ($Ra \leq 2 \times 10^{12}$; Stevens *et al.*, 2011). 2-D DNSs, however, support the existence of the ultimate regime (Zhu *et al.*, 2018).

For $Pr \ll 1$, the transition to the ultimate regime is expected at much lower Ra (Grossmann & Lohse, 2000). The critical value has been estimated as $Ra_* \simeq 10^{11}$ for $Pr \simeq 0.02$ (Chavanne *et al.*, 1997; Schumacher *et al.*, 2016; Ahlers *et al.*, 2017). 3-D DNSs have reached $Ra = 4 \times 10^8$, which is still in the classical regime (Schumacher *et al.*, 2016). To the best of our knowledge there is no DNS data available that would support or disprove the expected transition.

With this study we aim to contribute to the discussion by reporting numerical simulation results beyond transitional Ra for two Pr numbers. This is made feasible by utilizing the map-based, stochastic one-dimensional turbulence (ODT) model (Kerstein, 1999). We specifically limit our attention to Boussinesq fluids and smooth walls.

OVERVIEW OF THE ODT MODEL

The ODT computational domain is a statistically representative, vertical line of the turbulent flow as indicated in figure 1. There are no sidewall boundaries so that ODT simulations are performed for an RB cell with notionally infinite aspect ratio.

Stochastic simulations are performed with the temporal ODT formulation Kerstein (1999); Kerstein *et al.* (2001); Wunsch & Kerstein (2005). We have extended the model formulation of Wunsch & Kerstein (2005) to three velocity components (Kerstein *et al.*, 2001) within a dynamically-adaptive framework (Lignell *et al.*, 2013, 2018).

Governing Equations

The governing equations are the conservation equations of mass, momentum, and energy plus an equation of state. Here we make use of the Oberbeck–Boussinesq approximation with the linear equation of state, $\rho(T) = \rho_0 \left[1 - \beta\,(T - T_0)\right]$, where T is the temperature and ρ the weakly fluctuating density; the subscript 0 denotes background values. The density is therefore treated as constant except for the buoyancy forces. In this limit the ODT equations read (Wunsch & Kerstein, 2005):

$$\frac{\partial u_i}{\partial t} + \mathscr{E}_i(\alpha) = \nu \frac{\partial^2 u_i}{\partial z^2} \tag{3}$$

$$\frac{\partial T}{\partial t} + \mathscr{E}_T = \kappa \frac{\partial^2 T}{\partial z^2} \tag{4}$$

Here $(u_i) = (u, v, w)$ denotes the Cartesian velocity components, t the time and z the vertical coordinate, whereas $\mathscr{E}_i(\alpha)$ and $\mathscr{E}_T$ are stochastic terms that depend on the flow state. $\mathscr{E}_i(\alpha)$ models the effects of turbulent advection (Kerstein, 1999), buoyancy (Wunsch & Kerstein, 2005) and fluctuating pressure gradient forces (Kerstein *et al.*, 2001), whereas $\mathscr{E}_T$ only represents turbulent advection. The efficiency of pressure-velocity couplings is adjustable by the model parameter α, which takes values in between 0 and 1.

According to equations (3) and (4), molecular diffusion is treated as a continuous deterministic process, which is resolved in one dimension. The numerical solver uses a finite-volume-based discretization (Lignell *et al.*, 2013).

Stochastic Eddy Events

Deterministic diffusion is interrupted by instantaneous mapping (eddy) events. Each mapping consists of a permutation of fluid parcels across a randomly selected interval of the ODT line. This permutation is more generally described by a measure-preserving map yielding conservation of mass, momentum, and energy in an integral sense. The mapped flow profiles must be continuous and may only exhibit locally enhanced gradients.

These conservation and scale-locality properties are addressed by the triplet map (TM; Kerstein, 1999). For a given ODT line interval, $z_0 \leq z \leq z_1$, the TM (i) compresses flow profiles to a third of their length, (ii) pastes two copies to fill the line interval, and (iii) flips the central copy to ensure continuity. This algorithm is used in the adaptive ODT implementation in order to automatically increase the resolution in turbulent regions (Lignell *et al.*, 2013).

Eddy events are described by the random variables location z_0 and size $l = z_1 - z_0$ for a given time t. These variables have to be sampled from the eddy-rate distribution $\lambda(l, z_0; t) = l^{-2}\tau^{-1}(l, z_0; t)$, which depends on the flow state and is therefore unknown. A thinning-and-rejection method is used in practice to avoid the construction of the distribution function (Kerstein, 1999). The eddy rate τ^{-1} can be estimated from the flow state on energetic grounds. It follows from the eddy energy l^2/τ^2, which is given by (Kerstein, 1999; Wunsch & Kerstein, 2005):

$$\frac{l^2}{\tau^2} \simeq C^2 \frac{2}{\rho_0 V_\mathrm{e}} \left(\Delta E_\mathrm{kin} + \Delta E_\mathrm{pot} - Z E_\mathrm{vp}\right) \overset{!}{\geq} 0 \tag{5}$$

ΔE_kin and ΔE_pot denote the changes of the kinetic and the potential energy, respectively, due to the implementation of an eddy event of size l and V_e is the associated eddy volume. E_vp is a viscous penalty energy for the selected candidate event and implies energetic suppression of eddy events below the Kolmogorov scale (Kerstein, 1999). C is the eddy-rate and Z the small-scale (viscous) suppression parameter of the model. Candidate eddy events are deemed unphysical and rejected when $l^2/\tau^2 < 0$. Otherwise they are accepted with probability $\tau^{-1}/\tau_\mathrm{s}^{-1} \ll 1$, where τ_s^{-1} is the mean sampling rate (Kerstein, 1999). No large-scale suppression is used so that sizes up to $l/L = 1$ are permitted.

In our slightly extended formulation, the potential energy due to buoyancy is formally *released* to the vertical velocity component but can be redistributed simultaneously to the other components when $\alpha \neq 0$. In this case kinetic energy is also *taken* from all velocity components to obey energy conservation properties. Further technical details will be described elsewhere.

The model parameters C, Z, and α have to be estimated with the aid of reference data from DNS or measurements. This is addressed below.

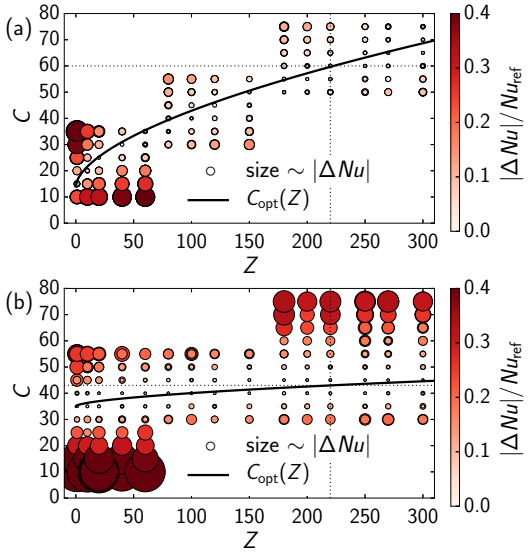

Figure 2. Model validation for the Nusselt number Nu. (a) $Pr = 0.7$, $Ra = (2.5 \pm 0.5) \times 10^{10}$, $Nu_{\mathrm{ref}} = 176 \pm 5$ (Stevens *et al.*, 2011; Li *et al.*, 2012); (b) $Pr = 0.021$, $Ra = 4 \times 10^8$, $Nu_{\mathrm{ref}} = 27.5 \pm 2.5$ (Schumacher *et al.*, 2016). Near-optimal values for C and Z are approximately given by $C_{\mathrm{opt}}(Z)$; the selected values are given by dotted lines.

RESULTS

In the following, we focus on the Ra-dependency of RB convection for $Pr = 0.021$ and 0.7, respectively. First, the ODT model parameters are estimated for each Pr. After that, these parameters are fixed in order to assess ODT's predictive capabilities.

Model Validation

The ODT model formulation has been validated for RB convection from a fundamental point of view by Wunsch & Kerstein (2005). Selecting $\alpha = 0$ recovers their ODT set-up except for a discrete evaluation of the mapping-kernel. We were able to reproduce relevant reference results. Next, we selected $\alpha = 2/3$ in order to introduce a tendency to small-scale isotropy as in Kolmogorov's turbulence by including pressure-velocity in the model Kerstein *et al.* (2001). Approximately the same Nusselt number Nu has been obtained for various model parameters C and Z irrespective of α. We fixed $\alpha = 2/3$ and compared ODT results to some available DNS data.

Figure 2 shows the difference $\Delta Nu = Nu - Nu_{\mathrm{ref}}$ between the ODT and reference Nusselt numbers for various model parameters C and Z. Various parameter combinations yield the same Nu or, likewise, the same wall temperature gradient. These combinations are described by the empirical curves $C_{\mathrm{opt}}(Z) = 2.0\, Z^{0.58} + 14$ for $Pr = 0.7$, and $C_{\mathrm{opt}}(Z) = 0.35\, Z^{0.58} + 35$ for $Pr = 0.021$.

It remains to fix Z and C by an additional criterion. We recall from equation (5) that Z is related to viscous effects. By assuming further that the turbulent boundary layer dynamics are universal, Z has been estimated by matching the logarithmic region of the mean temperature profile. This was done only once for $Pr = 0.7$, $Ra = (2.5 \pm 0.5) \times 10^{10}$ (see figure 5(a); and Klein *et al.*, 2018, for further details). The physical model parameters selected by this procedure are given by $\alpha = 2/3$, $Z = 220$, $C = 60$ for $Pr = 0.7$, and $C = 43$ for $Pr = 0.021$.

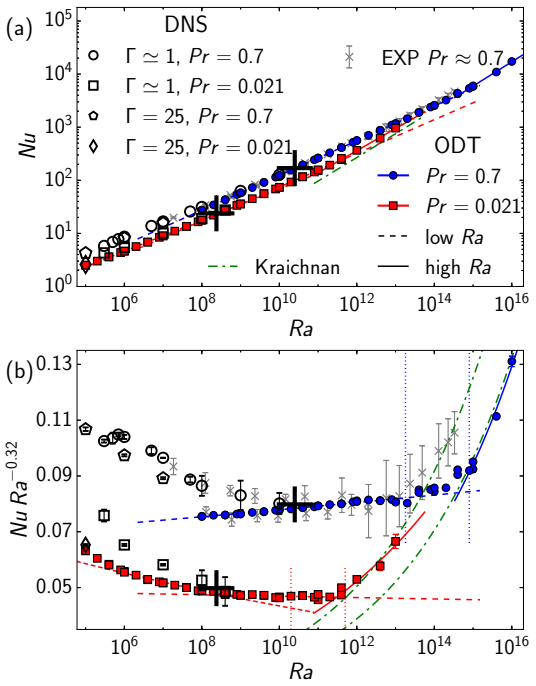

Figure 3. (a) Scaling of the Nusselt number Nu versus Rayleigh number Ra for the Prandtl numbers $Pr = 0.7$ and 0.021. (b) Same data but compensated with $Ra^{0.32}$. ODT results and the corresponding scaling laws are given in blue and red. Reference DNS data (black) is given for $1 \leq \Gamma \leq 3$, $Pr = 0.7$ (Scheel & Schumacher, 2014); $\Gamma = 1$, $Pr = 0.021$ (Scheel & Schumacher, 2016; Schumacher *et al.*, 2016); $\Gamma = 25$, $Pr = 0.7$ and 0.021 (Pandey *et al.*, 2018). Reference measurement data (EXP, gray) encompasses $0.23 \leq \Gamma \leq 20$, $0.5 \leq Pr \leq 10$ as compiled in Chillà & Schumacher (2012). The ultimate scaling according to Kraichnan (1962) is given by dash-dotted lines with arbitrary prefactors. Expected transition ranges in terms of Ra are marked by dotted lines. Thick crosses mark the ODT validation cases (figure 2).

Nusselt Number

The dependence $Nu(Ra, Pr)$ is investigated for $Pr = 0.7$ and 0.021 by stochastic ODT simulations. The ODT model parameters are kept constant to address the predictive capabilities of the model. Nu is computed according to equation (2) for the 1-D computational domain by long-time averaging over several million eddy events in the statistically stationary state. Confidence margins are obtained by computing Nu in the upper and lower half of the domain only. The Rayleigh numbers investigate encompass $10^8 \leq Ra \leq 10^{16}$ $Pr = 0.7$ and $10^5 \leq Ra \leq 10^{13}$ for $Pr = 0.021$.

Figure 3 shows the Nusselt number Nu as a function of the Rayleigh number Ra for both Prandtl numbers Pr investigated. ODT simulation results are compared to reference data from DNS and laboratory measurements, which encompass a range of aspect ratios and Prandtl numbers. For very large Ra, however, there is no reference data so that we show the theoretical scaling $Nu \propto Ra^{1/2}\ [\log(Ra)]^{-3/2}$ according to Kraichnan (1962). The Nusselt numbers shown in figure 3(a) exhibit very good agreement between ODT and the available reference values across eight decades of Ra for each Pr. This agreement is more of a qualitative nature since the range of Nu is rather large.

Table 1. Effective scaling laws $Nu \propto Ra^{\gamma}$ for various ranges $Ra_{\min} \le Ra \le Ra_{\max}$. Corresponding reference values γ_{ref} are from Scheel & Schumacher (2014, 2016, †), Shraiman & Siggia (1990, ∗), and Kraichnan (1962, ‡).

Pr	$Ra_{\min}$	$Ra_{\max}$	γ_{ODT}	γ_{ref}
0.021	10^6	5×10^8	0.29(1)	$0.26(1)^{\dagger}$
0.021	10^9	5×10^{11}	0.32(1)	$0.28(1)^{*}$
0.021	4×10^{11}	2×10^{13}	0.40(2)	$0.448^{\ddagger}$
0.7	10^8	10^{13}	0.32(1)	$0.29(1)^{\dagger}$
0.7	8×10^{14}	10^{16}	0.44(1)	$0.458^{\ddagger}$

The comparison between ODT simulated Nu and reference data is made more quantitative in figure 3(b) by showing data compensated with $Ra^{0.32}$. This gives a better impression of the confidence margins that are within the symbol size if they are not visible. The ODT data exhibit various effective scaling laws. These have been obtained by a least-squares fit and are summarized in table 1.

For $Ra < 10^{13}$ ($Pr = 0.7$) and $Ra < 10^9$ ($Pr = 0.021$), ODT exhibits the classical scaling close to $Nu \propto Ra^{1/3}$ in agreement with Malkus (1954). A relative decrease of the exponent for $Ra < 10^9$ to $Nu \propto Ra^{2/7}$ (Shraiman & Siggia, 1990) is only observed for $Pr = 0.021$. For this Pr, the ODT simulated Nu for $Ra = 10^5$ agrees with the reference value of Pandey *et al.* (2018) that has been obtained for a large-aspect-ratio RB cell ($\Gamma = 25$). This suggests that the ODT formulation is consistent with $\Gamma \gg 1$ and, thus, complementary to DNS and laboratory experiments that exhibit $\Gamma \lesssim 1$. We conjecture that geometrical, small-aspect-ratio effects (like the unresolved large-scale circulation) are the main reason for the different scaling observed for $Ra < 10^9$ ($Pr = 0.7$).

The transition to the ultimate state of convection is expected for $1.8\times10^{13} \le Ra \le 8\times10^{14}$ ($Pr = 0.7$; He *et al.*, 2012) and $2\times10^{10} \le Ra \le 5\times10^{11}$ ($Pr = 0.021$; Schumacher *et al.*, 2016; Ahlers *et al.*, 2017). These ranges are marked with dotted lines in figure 3(b) and, indeed, a transition has been observed in many experiments for $\Gamma = O(1)$ and $Pr = O(1)$. It is remarkable that the present ODT results exhibit the expected transition within the expected range of Ra for the unchanged model configuration. For even larger Ra, present ODT results exhibit the onset of the Kraichnan (1962) scaling. Only the prefactor retains a dependence on Pr. Table 1 summarizes these results in terms of $Nu \propto Ra^{\gamma}$ scalings. ODT weakly overestimates (underestimates) the exponent γ expected for the classical (ultimate) regime.

The critical Ra_* obtained with ODT are at the upper end of the expected transition ranges, that is, $Ra_* \simeq 6\times10^{14}$ ($Pr = 0.7$) and $Ra_* \simeq 6\times10^{11}$ ($Pr = 0.021$). We note that the aspect ratio might influence Ra_* due to the presence, or absence, of a large-scale circulation. In ODT, any mean circulation is absent by construction (see figure 4).

Bulk Profiles

Figure 4 shows profiles of the instantaneous and mean temperature together with profiles of a wall-tangential velocity component for the two Prandtl numbers investigated. The selected cases exhibit approximately the same Grashof number $Gr = Ra/Pr = (1.6\pm0.3)\times10^{10}$. The spatial scales in the instantaneous velocity fields are therefore comparable for both cases. They are also similar to the spatial scales in the temperature field since the diffusion time scales are similar for $Pr \simeq 1$. By contrast, the spatial scales are larger in the temperature field for the lower $Pr = 0.021$, which is due to the faster thermal than viscous diffusion.

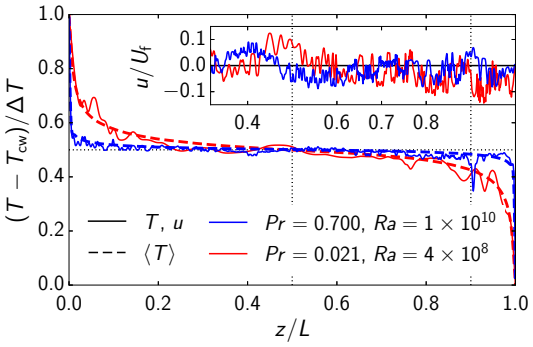

Figure 4. Vertical profiles of the instantaneous T and time-averaged temperature $\langle T \rangle$ together with the instantaneous wall-tangential velocity u (inset). Two cases with different Pr but similar $Gr = (1.6\pm0.3)\times10^{10}$ are shown. $U_f = \sqrt{g\beta\Delta T L}$ is the free-fall velocity. Vertical dotted lines are given for orientation.

The mean temperature profile is smooth, monotonic and symmetric to $(0.5, 0.5)$. The mean velocity is zero since ODT does not resolve the cell-like structure for $\Gamma \to \infty$.

Low-Order Temperature Statistics

Vertical profiles of first and second order temperature statistics have been obtained by temporal averaging in the statistically stationary state. This yielded:

$$\Theta(z) = \big(\langle T\rangle(z) - T_b\big)\Big/\Delta T \tag{6}$$

$$\sigma(z) = \sqrt{\langle T^2\rangle(z) - \langle T\rangle^2(z)}\Big/\Delta T \tag{7}$$

In these equations, $\langle\cdot\rangle$ denotes the temporal average, Θ the non-dimensional mean temperature, σ the non-dimensional standard deviation of the temperature fluctuations, and $T_b = (T_{hw} + T_{cw})/2$ the bulk temperature.

Figures 5 and 6 show low-order temperature statistics for $Pr = 0.7$ and 0.021, respectively. Reference DNS data are available in the classical regime and these are shown for comparison. The flow statistics are symmetric to the mid-height so that we present data for the lower half of the domain ($0 \le z/L \le 0.5$). The thermal boundary layer thickness $\delta/L = (2\,Nu)^{-1}$ is given for orientation. Geometrically, δ is given by the intersection of the linearly extrapolated wall-temperature gradient, $z\,(\mathrm{d}\Theta/\mathrm{d}z)_{hw} + 0.5$, and the horizontal axis $\Theta = 0$ since the temperature flux is carried entirely by molecular diffusion next to the wall. Note that σ has been normalized by its maximum value σ_{max} in figures 5(b) and 6(b) in order to focus on the shapes.

In general, Θ and σ are well captured by ODT for both Pr, in the vicinity of the wall and further towards the bulk. For $Pr = 0.7$ (figure 5) one can discern a spurious, undulating structure in the ODT results for finite distance from the wall, $2\times10^{-3} \lesssim z/L \lesssim 10^{-2}$. This feature is a modeling artifact that is related to the triplet mapping (Lignell

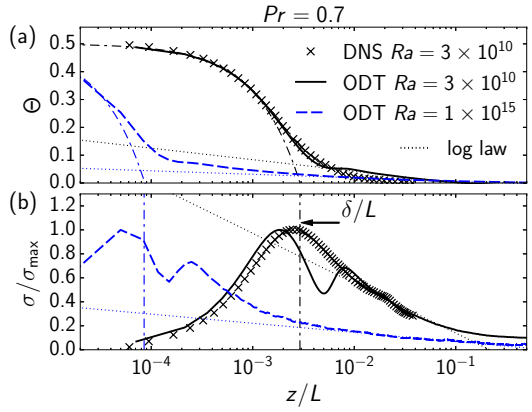

Figure 5. Thermal boundary layer for $Pr = 0.7$. (a) Non-dimensional mean temperature Θ for the bottom half of the domain. Dash-dotted lines give the linear extrapolation of the wall gradient. (b) Standard deviation σ of the temperature fluctuations. Vertical dash-dotted lines mark the thermal boundary layer thickness δ. Dotted lines are fits to the logarithmic region. Reference DNS data is from Li *et al.* (2012) for the centerline of a cylindrical cell with $\Gamma = 1$.

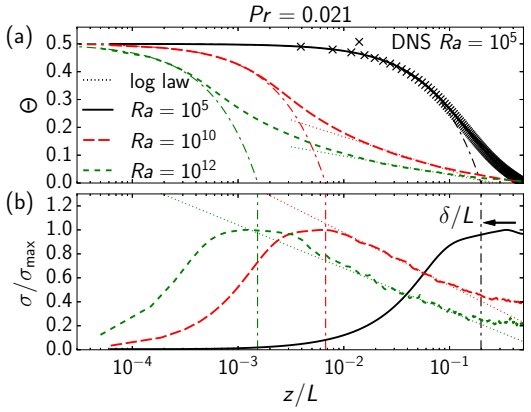

Figure 6. Similar to figure 5 but for $Pr = 0.021$. Reference DNS data is from Pandey *et al.* (2018) for a rectangular cell with $\Gamma = 25$.

et al., 2013; Klein & Schmidt, 2017). Interestingly, this artifact has disappeared for $Pr = 0.021$ as can be seen in figure 6. We attribute this effect to the thermal diffusivity, which is larger for lower Pr. In addition, the turbulence is also more vigorous and, considering the velocity field, exhibits a broader range of scales. So, not only molecular but also turbulent processes diffuse the imprint of the TM. This is consistent with the effects of a reduced ODT small-scale suppression parameter Z (see Klein *et al.*, 2018).

Both Θ and σ exhibit a logarithmic region when Ra is large enough. This region is described by:

$$\Theta(z) = A\,\ln(z/L) + B \qquad \sigma(z) = C\,\ln(z/L) + D \qquad (8)$$

The coefficients A, B, C, D have been obtained by a least-squares fit for the interval $10^{-2} \leq z/L \leq 10^{-1}$. These fits are given by dotted lines in figures 5 and 6, where the case with $Pr = 0.021$, $Ra = 10^5$ was excluded since it does not exhibit a logarithmic region. Nevertheless, the coefficients A and C approach zero for increasing Ra which is in qualitative agreement with Ahlers *et al.* (2012).

Turbulent Temperature Flux

The turbulent temperature flux density $\langle w'T' \rangle$ is computed in ODT on the basis of the map-induced changes in an operator-splitting fashion. Therefore, cross-correlations are typically captured rather well by the lower-order ODT model even when the autocorrelation of the fluctuating quantities is underestimated (e.g. Kerstein, 1999; Kerstein *et al.*, 2001; Klein *et al.*, 2019). We make use of this property of the ODT model to gain further insight into RB convection in the ultimate compared to the classical regime.

Figure 7 shows vertical profiles of the time-averaged turbulent temperature flux density $\langle w'T' \rangle$ obtained with ODT for the lower half of the domain. The data have been normalized with the maximum value $\langle w'T' \rangle_{\max}$ in order to focus on the shapes. In the classical regime, for $Pr = 0.7$, $Ra = 3 \times 10^{10}$ in figure 7(a), $\langle w'T' \rangle$ increases rapidly across the diffusive sublayer so that the maximum value is reached

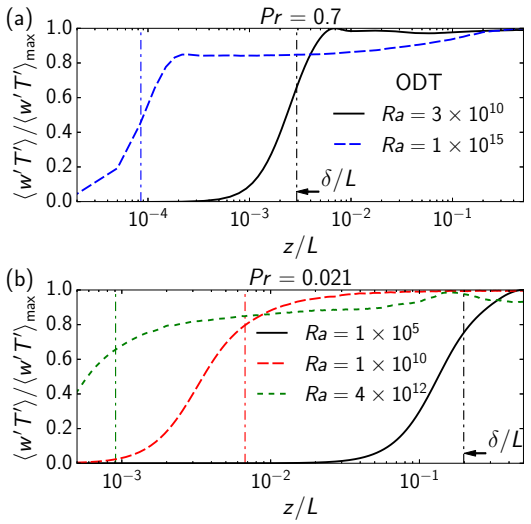

Figure 7. Turbulent temperature flux density $\langle w'T' \rangle$ across the boundary layer. (a) $Pr = 0.7$; (b) $Pr = 0.021$. Vertical dash-dotted lines mark the thermal boundary layer thickness δ due to the slope method.

at $z/L \approx 2\delta/L \approx 6 \times 10^{-3}$. This is similar for the case $Pr = 0.021$, $Ra = 10^{10}$ in figure 7(b).

By contrast, in the ultimate regime, for $Pr = 0.7$, $Ra = 10^{15}$ in figure 7(a), $\langle w'T' \rangle$ has only reached $\approx 82\%$ of its maximum value at $z/L = 2\delta/L \approx 2 \times 10^{-4}$. The turbulent flux increases further with distance, but more gradually, and attains its maximum value in the bulk for $z/L \gtrsim 0.2$. A similar behavior can be discerned in figure 7(b) for $Pr = 0.021$, $Ra = 4 \times 10^{12}$. Here $\langle w'T' \rangle$ reaches only $\approx 75\%$ of its maximum value at $z/L = 2\delta/L \approx 2 \times 10^{-3}$. Interestingly, the maximum turbulent flux is reached around $z/L \approx 0.15$ in the present ODT results, but reduces again towards the mid-height. This effect is robustly observed also for a higher Ra investigated.

Note that the case $Pr = 0.021$, $Ra = 10^5$ is dominated by thermal diffusion. The sublayer extends up to $z/L = 2\delta/L \approx 0.4$ and $\langle w'T' \rangle$ peaks at mid-height.

Note further that the shape differences of $\langle w'T' \rangle$ between the cases $Pr = 0.7$, $Ra = 3 \times 10^{10}$ and $Pr = 0.021$, $Ra = 10^{10}$ across $10^{-3} \leq z/L \leq 10^{-2}$ are presumably related to the TM (see the discussion of figures 5 and 6).

CONCLUSION

Stochastic one-dimensional turbulence (ODT) simulations of low-Pr convection have been performed in order to address the transition from the classical to the ultimate regime. A Boussinesq fluid between smooth isothermal no-slip walls has been considered in a set-up with infinite aspect ratio. We have shown that ODT is able to capture the classical $Nu \propto Ra^{1/3}$ scaling (Malkus, 1954) as well as the onset of the ultimate $Nu \propto Ra^{1/2}$ scaling (Kraichnan, 1962) for fixed model parameters. The critical Rayleigh numbers Ra_* are also captured. ODT yields $Ra_* \simeq 6 \times 10^{14}$ ($Pr = 0.7$) and $Ra_* \simeq 6 \times 10^{11}$ ($Pr = 0.021$). These values are within the transition ranges given in the literature (He *et al.*, 2012; Schumacher *et al.*, 2016; Ahlers *et al.*, 2017).

Furthermore, the present ODT results exhibit a turbulent (logarithmic) boundary layer before and after the transition. After the onset of the ultimate regime, however, molecular-diffusive contributions to the temperature flux are no longer negligible outside the thermal sublayer. This appears to be a consequence of the strongly developed logarithmic region by which fluid is transported efficiently over large distances in the wall-normal vertical direction.

The results obtained indicate very reasonable predictive capabilities of ODT and give a glimpse at the potential of physics-based, stochastic turbulence models.

ACKNOWLEDGEMENTS

We thank Ambrish Pandey for providing DNS data. Funding: European Regional Development Fund (EFRE), No. StaF 23035000; German Academic Exchange Service (DAAD), which is funded by the Federal Ministry of Education and Research (BMBF), No. ID-57316240.

REFERENCES

Ahlers, G., Bodenschatz, E., Funfschilling, D., Grossmann, S., He, X., Lohse, D., Stevens, R. J. A. M. & Verzicco, R. 2012 Logarithmic temperature profiles in turbulent Rayleigh–Bénard convection. *Phys. Rev. Lett.* **109**, 114501.

Ahlers, G., Bodenschatz, E. & He, X. 2017 Ultimate-state transition of turbulent Rayleigh–Bénard convection. *Phys. Rev. Fluids* **2**, 054603.

Chavanne, X., Chillà, F., Castaing, B., Hébral, B., Chabaud, B. & Chaussy, J. 1997 Observation of the ultimate regime in Rayleigh–Bénard convection. *Phys. Rev. Lett.* **79** (19), 3648–3651.

Chillà, F. & Schumacher, J. 2012 New perspectives in turbulent Rayleigh–Bénard convection. *Eur. Phys. J. E* **35**, 58.

Grossmann, S. & Lohse, D. 2000 Scaling in thermal convection: A unifying theory. *J. Fluid Mech.* **407**, 27–56.

He, X., Funfschilling, D., Nobach, H., Bodenschatz, E. & Ahlers, G. 2012 Transition to the ultimate state of turbulent Rayleigh–Bénard convection. *Phys. Rev. Lett.* **108**, 024502.

Kerstein, A. R. 1999 One-dimensional turbulence: Model formulation and application to homogeneous turbulence, shear flows, and buoyant stratified flows. *J. Fluid Mech.* **392**, 277–334.

Kerstein, A. R., Ashurst, W. T., Wunsch, S. & Nilsen, V. 2001 One-dimensional turbulence: Vector formulation and application to free shear flows. *J. Fluid Mech.* **447**, 85–109.

Klein, M. & Schmidt, H. 2017 Stochastic modeling of passive scalar transport in turbulent channel flows at high Schmidt numbers. In *Proc. 10th Int. Symp. Turb. Shear Flow Phen. (TSFP10)*, pp. 1–5 (1B–2). Chicago, IL.

Klein, M., Schmidt, H. & Lignell, D. O. 2018 Map-based modeling of high-Rayleigh-number turbulent convection in planar and spherical confinements. In *Proc. Conf. Model. Fluid Flow (CMFF'18)* (ed. J. Vad). Budapest, Hungary, ISBN 978-963313297-5.

Klein, M., Zenker, C. & Schmidt, H. 2019 Small-scale resolving simulations of the turbulent mixing in confined planar jets using one-dimensional turbulence. *Chem. Eng. Sci.* **204**, 186–202.

Kraichnan, R. H. 1962 Turbulent thermal convection at arbitrary Prandtl number. *Phys. Fluids* **5**, 1374.

Li, L., Shi, N., du Puits, R., Resagk, C., Schumacher, J. & Thess, A. 2012 Boundary layer analysis in turbulent Rayleigh–Bénard convection in air: Experiment versus simulation. *Phys. Rev. E* **86**, 026315.

Lignell, D. O., Kerstein, A. R., Sun, G. & Monson, E. I. 2013 Mesh adaption for efficient multiscale implementation of one-dimensional turbulence. *Theor. Comp. Fluid Dyn.* **27** (3), 273–295.

Lignell, D. O., Lansinger, V., Medina, J., Klein, M., Kerstein, A. R., Schmidt, H., Fistler, M. & Oevermann, M. 2018 One-dimensional turbulence modeling for cylindrical and spherical flows: Model formulation and application. *Theor. Comp. Fluid Dyn.* **32** (4), 495–520.

Malkus, W. V. R. 1954 Discrete transitions in turbulent convection. *Proc. Royal Soc. A* **225**, 185–195.

Pandey, A., Scheel, J. D. & Schumacher, J. 2018 Turbulent superstructures in Rayleigh–Bénard convection. *Nature Comm.* **9**, 2118.

Scheel, J. D. & Schumacher, J. 2014 Local boundary layer scales in turbulent Rayleigh–Bénard convection. *J. Fluid Mech.* **758**, 344–373.

Scheel, J. D. & Schumacher, J. 2016 Global and local statistics in turbulent convection at low Prandtl numbers. *J. Fluid Mech.* **802**, 147–173.

Schumacher, J., Bandaru, V., Pandey, A. & Scheel, J. D. 2016 Transitional boundary layers in low-Prandtl-number convection. *Phys. Rev. Fluids* **1**, 084402.

Shraiman, B. I. & Siggia, E. D. 1990 Heat transport in high-Rayleigh-number convection. *Phys. Rev. A* **42** (6), 3650–3653.

Stevens, R. J. A. M., Lohse, D. & Verzicco, R. 2011 Prandtl and Rayleigh number dependence of heat transport in high Rayleigh number thermal convection. *J. Fluid Mech.* **688**, 31–43.

Urban, P., Hanzelka, P., Králík, T., Macek, M., Musilová, V. & Skrbek, L. 2019 Elusive transition to the ultimate regime of turbulent Rayleigh–Bénard convection. *Phys. Rev. E* **99**, 011101(R).

Wunsch, S. & Kerstein, A. R. 2005 A stochastic model for high-Rayleigh-number convection. *J. Fluid Mech.* **528**, 173–205.

Zhu, X., Mathai, V., Stevens, R. J. A. M., Verzicco, R. & Lohse, D. 2018 Transition to the ultimate regime in two-dimensional Rayleigh–Bénard convection. *Phys. Rev. Lett.* **120**, 144502.

Zhu, X., Stevens, R. J. A. M., Shishkina, O., Verzicco, R. & Lohse, D. 2019 $Nu \sim Ra^{1/2}$ scaling enabled by multiscale wall roughness in Rayleigh–Bénard turbulence. *J. Fluid Mech.* **869**.